Surgenor

Details of a Study of
Interfacial Momentum Transfer in Two-Phase
Two-Component Critical Flows

M.Eng.

DETAILS OF A STUDY OF

INTERFACIAL MOMENTUM TRANSFER IN TWO-PHASE

TWO-COMPONENT CRITICAL FLOWS *

by

BRIAN W. SURGENOR, B.Eng.

A Report Submitted to the School of Graduate Studies

in Partial Fulfillment of the Requirements

for the Degree

Master of Engineering

Department of Engineering Physics

McMaster University

Hamilton, Ontario, L8S 4M1, Canada

January, 1979

MASTER OF ENGINEERING (1979)
Department of Engineering Physics

TITLE: Details of a Study of
                      Interfacial Momentum Transfer in Two-Phase
                      Two-Component Critical Flows

AUTHOR: Brian W. Surgenor, B.Eng. (Queen's)

SUPERVISOR: Dr. T.R. Heidrick

NUMBER OF PAGES: ix, 58

ABSTRACT

Preparations for an investigation of interfacial momentum transfer in two-phase two-component critical flows have been completed.

The experiments involve the measurement of flow rates, axial pressure profiles, axial and transverse void fraction profiles, and axial wall shear stress profiles of steady-state gas-liquid critical flow in a vertical diverging nozzle. A photographic study is to be initiated to record the flow structure. The results of these experiments will be used to develop constitutive relations for interfacial momentum transfer.

An experimental loop capable of circulating a gas-liquid mixture in a vertical test section was modified to suit the requirements of this investigation. The void fraction profiles are measured with a traversing gamma densitometer using a 20 mCi Co^{57} source. The wall shear stress profiles are obtained using the electrochemical method to measure the mass transfer coefficients of electrodes mounted flush with the test section wall. The liquid phase is an electrolyte and the gaseous phase can be air, nitrogen or freon. The latter is used to better approximate the densities of a steam-water flow.

This report describes the required theory, measurement techniques, design and operation of the loop, and the experimental procedures.

ACKNOWLEDGEMENTS

TABLE OF CONTENTS

LIST OF TABLES

LIST OF FIGURES

CHAPTER 1

INTRODUCTION

Accurate analytical models of transient two-phase flows are required to evaluate the effectiveness of nuclear reactor core cooling systems. An advanced model under development by reactor safety concerns is the separated flow model, in which the conservation equations of mass, momentum and energy are written separately for each phase. Interphase constitutive relations are required to account for the interaction between the phases. This investigation is directed at the need to develop accurate relations for interfacial momentum transfer.

When a fluid escapes from a high pressure reservoir to low pressure surroundings, the flow rate first increases as the differential pressure between the reservoir and the surroundings is increased, typically by lowering the pressure of the latter. Continued lowering of the surroundings' pressure will result in a maximum flow rate. This maximum value cannot be exceeded by further reduction of the pressure of the surroundings. This condition is known as 'critical flow' or 'choked flow'. It is said to occur at the 'critical flow plane'.

Critical flow is characterized by very steep pressure gradients downstream of the critical flow plane. It is this

property which leads to the application of critical flow in
this investigation. Under normal flow conditions, inter-
facial momentum transfer is a relatively small component of
the total momentum transfer. It is unlikely that experimental
data would be sufficiently accurate to enable evaluation of
the constitutive relation for interfacial momentum transfer
to the degree of detail desired. However in critical flow
the light gas phase is rapidly accelerated over the heavier
liquid phase, due to the steep pressure gradients. Interfacial
effects would be expected to dominate the flow. Thus in
critical flow, interfacial momentum transfer should form a
large component of the total momentum transfer, making
evaluation of the constitutive relation more effective.

Preliminary to the actual investigation, an existing
test facility had to be redesigned. A loop was rebuilt to
enable circulation of a gas-liquid mixture through a vertical
test section under critical flow conditions. The test section
is a diverging nozzle instrumented for measurement of the
axial pressure profiles, axial and transverse void fraction
profiles, and wall shear stress profiles. Having measured
these parameters, together with the flow rates, the interfacial
shear terms can be calculated from the momentum conservation
equations and the interfacial momentum transfer so evaluated.
The void fraction is measured with a traversing gamma
densitometer using a 20 mCi Co^{57} source. The electrochemical
method is used to obtain the wall shear stress by measuring

the mass transfer coefficients of electrodes mounted flush with the test section wall. The test section is transparent to enable photographs of the flow structure to be taken.

This report serves to fully describe the experimental apparatus, measuring techniques, required theory and operating procedures.

CHAPTER 2

THEORY

In any discussion of two-phase flow, one must make reference to the flow regime, that is the relative distribution and motion of the phases. The principal regimes in vertical flow are illustrated in Figure 2-1 (1). Descriptions in order of their appearance with increasing gas flow are:

1. Bubbly flow, in which the liquid forms a continuous phase, with the gas dispersed as small individual bubbles.

2. Slug flow, in which the gas flows as large bullet shaped bubbles, separated by slugs of liquid.

3. Churn flow, which forms a transition regime between the more permanent slug and annular regimes. It is characterized by an oscillatory motion of the liquid slugs.

4. Annular flow, in which the gas flows as a continuous phase in the core, with the liquid travelling as an annular film on the wall. Some liquid can be entrained as droplets in the gas core.

The basic theory required for analysis of the experimental data is given in this chapter. In the first section the momentum equations based upon the separated flow
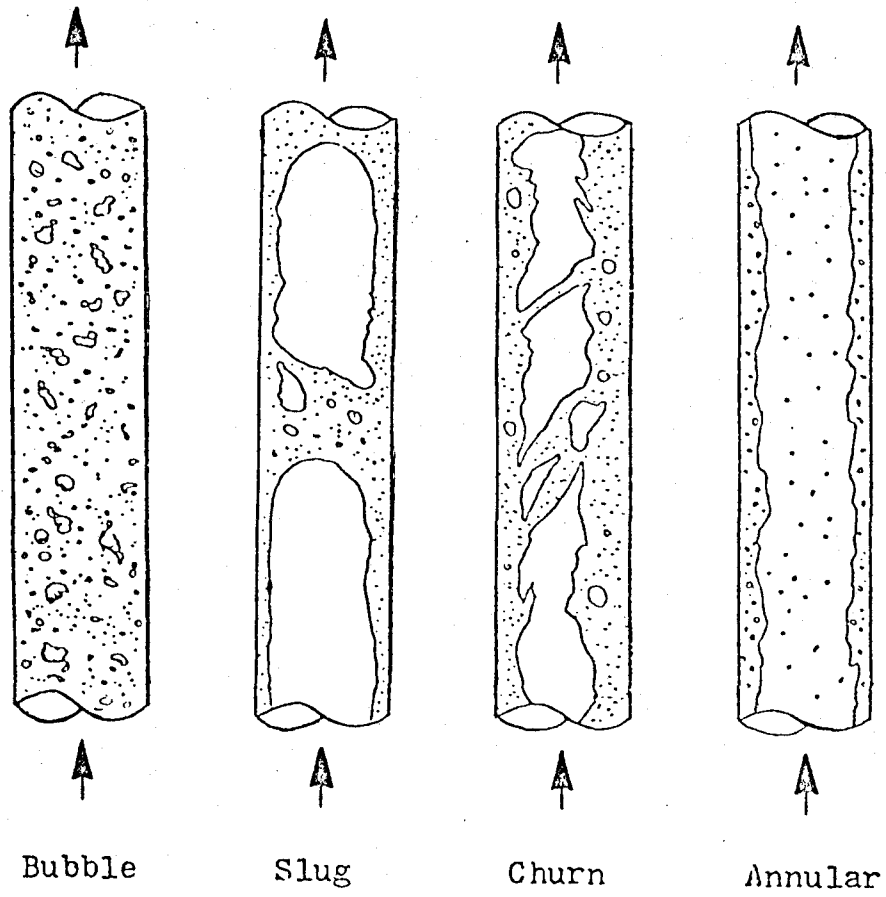
Fig. 2-1. Flow regimes in vertical cocurrent flow.

model are presented, together with a further discussion of interfacial momentum transfer. The second section provides three models for the prediction of the critical mass flux. The last two sections give the theory underlying the wall shear stress and void fraction measurements.

2.1   Momentum Equations

The momentum equations for a two-component two-phase flow are presented in their final form as derived from the conservation equations of the separated flow model. For the original equations, one can refer to the form presented by Banerjee and Hancox (2).

The underlying assumptions and simplifications for these equations are given below.

1. The flow is one-dimensional, vertical, adiabatic and steady.

2. There is no interfacial heat or mass transfer.

3. The wall is continuously wetted, thus there is no wall shear acting on the gas phase.

4. The gas and liquid phase pressures are equal. In addition, the interfacial phase pressures and bulk phase pressures are equal.

5. All variables are represented in the equations as cross-sectional averages.

6. The mass flux is constant along the length ∂z, thus $\partial G / \partial z = 0$. This follows from the mass conservation equation. A required condition is a constant

cross-sectional area along ∂z.

The momentum equation for the liquid component is

$$- (1 - \propto) \frac{\partial P}{\partial z} = (1 - \propto) \rho_1 g + G_1 \frac{\partial u_1}{\partial z} - \frac{\tau_i a_i}{A\,L} + \frac{\tau_w a_w}{A\,L} \qquad (2.1)$$

The momentum equation for the gas component is

$$- \propto \frac{\partial P}{\partial z} = \propto \rho_g g + G_g \frac{\partial u_g}{\partial z} + \frac{\tau_i a_i}{A\,L} \qquad (2.2)$$

The combined equation is

$$- \frac{\partial P}{\partial z} = \left[(1 - \propto) \rho_1 + \propto \rho_g \right] g + \left[G_1 \frac{\partial u_1}{\partial z} + G_g \frac{\partial u_g}{\partial z} \right]$$

$$+ \frac{4\,\tau_w}{d} \qquad (2.3)$$

The three terms on the right side of this equation are the gravitational, accelerational and frictional components of the pressure drop, respectively.

An important assumption has been that the forces exerted on the phases by each other can be given by the interfacial shear term $\tau_i a_i$, acting equally and in opposite directions, and containing no derivative terms. The interfacial shear term represents the interphase momentum transfer constitutive relation and can be considered to be made up of two components:

1. The frictional force, analogous to the force exerted at the wall in single-phase flow.

2. The force due to the interference between the phases. One phase must be displaced by the other if

they are moving in different directions or possess different velocities. This component is referred to as the 'added mass' or 'virtual mass' term and is essentially a two-dimensional effect.

The second component is generally ignored and a typical constitutive relation for the interfacial shear stress is that proposed by Wallis for annular flow (3)

$$\tau_i = 0.0025 \, (1 + 75(1 - \alpha)) \, \rho_g \, u_g^2 \qquad (2.4)$$

and the similarity of the relation to formulas for the wall shear stress in single-phase flow is self-evident. The interfacial area is calculated using

$$a_i = \pi D L \, (\alpha)^{\frac{1}{2}} \qquad (2.5)$$

having assumed a smooth interface between the annular liquid film and the gas core, with no liquid entrainment. The success of relations such as Wallis' indicates that under normal conditions, the dominant interfacial force is one of friction and not displacement. However the virtual mass term should not be ignored in strongly accelerated flows, as would be experienced in critical flow.

With equations (2.1) and (2.2) the interfacial shear terms can be calculated from the measured void fractions, pressure drops, wall shear stresses and flow rates. Any inconsistency in these interfacial shear terms would indicate the need to re-evaluate their form and underlying assumptions.

Effects such as those of virtual mass and the presence of derivative terms in the interfacial shear terms might have to be considered. The objective of this investigation is the evaluation of these effects and to subsequently determine accurate constitutive relations for interfacial momentum transfer for the different flow regimes.

2.2   Critical Flow Models

As the critical flow condition determines the maximum possible escape rate of a high pressure fluid from its containment, it has a direct and very important application to nuclear reactor safety. The phenomenon represents the highest rate at which the coolant can be lost from the reactor coolant system in the event of a pipe break. This escape rate in turn fixes the pressure within the containment building. Consequently a great many experimental and analytical studies of two-phase critical flow have been performed in the past and are being performed in the present. The paper by Boure et al (4) presents a comprehensive theoretical analysis of the subject. Hsu and Graham's book (5) reviews the various models available to predict critical flows and their relative agreement with experiment.

A number of criteria can be applied to define the onset and existence of critical flow. The most general criteria is that no 'disturbances' can propagate upstream of the critical flow plane. Thus variables such as the pressure drop or the flow rate are unaffected by events downstream of

the plane and will exhibit the behaviour illustrated in Figure 2-2a and 2-2b. Critical flow has been characterized in the separated flow model as the point of maximum slip between the gas and liquid phases (6). In a strict analytical analysis a step by step integration procedure of the governing equations can be performed, marching downstream to the point at which the derivatives become infinite, so arriving at the critical flow plane. If one is working with the complete set of differential equations for the separated flow model (two mass, two momentum, two energy) this point would be indicated by the sixth-order system determinant going to zero (4).

Critical flow occurs in both single- and two-phase systems. Single-phase critical flow occurs when the exit velocity at the point of choking equals the local sound velocity. This corresponds to about 1,500 m/s for liquid water and 500 m/s for water vapour. Critical velocities in two-phase flow can be in the 50 m/s range, with the individual phase velocites being considerably lower than their corresponding sonic velocities.

Consider the condition that critical flow is determined when the flow rate no longer increases with decreasing down-stream pressure (5, p. 335). Thus

$$\partial G / \partial P = 0 \qquad\qquad (2.6)$$

In critical flow, the frictional and gravitational components can be neglected for a good approximation of the pressure

Test Section Profile

Throat

Pressure

Onset of
Critical
Flow

Exit
Pressure
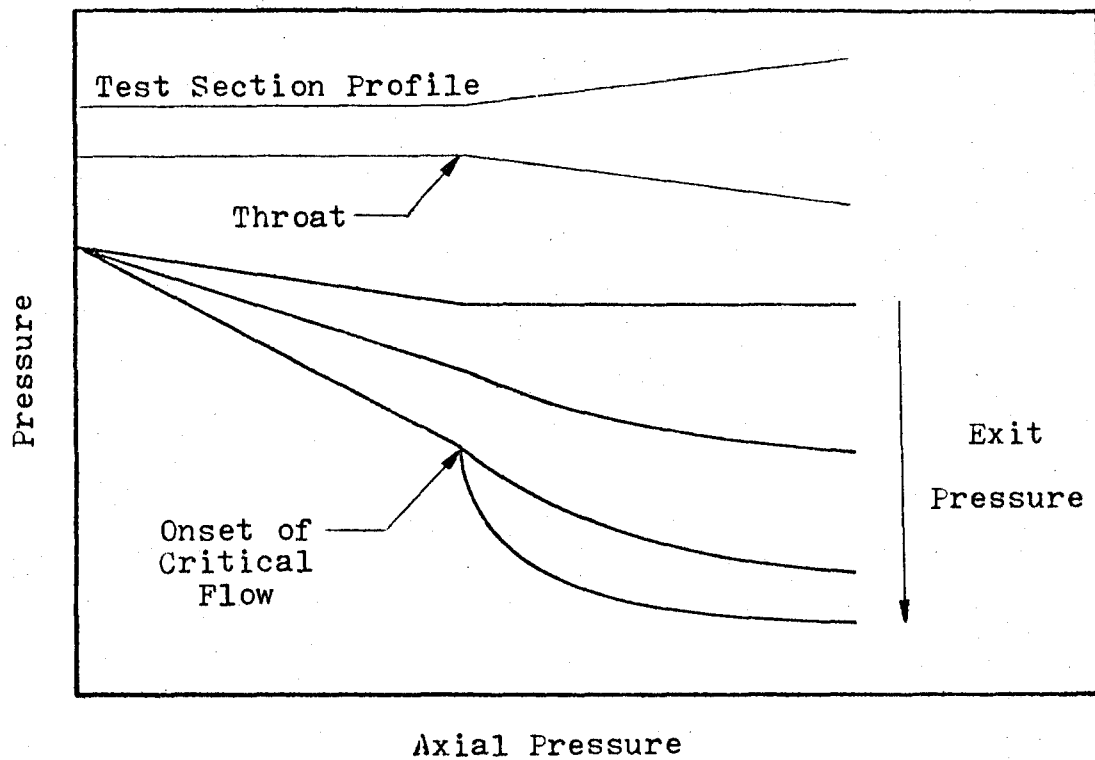
Axial Pressure

Fig. 2-2a.   Variation of axial pressure profile with exit
pressure, showing onset of critical flow.

Onset of
Critical
Flow

Mass Flow Rate
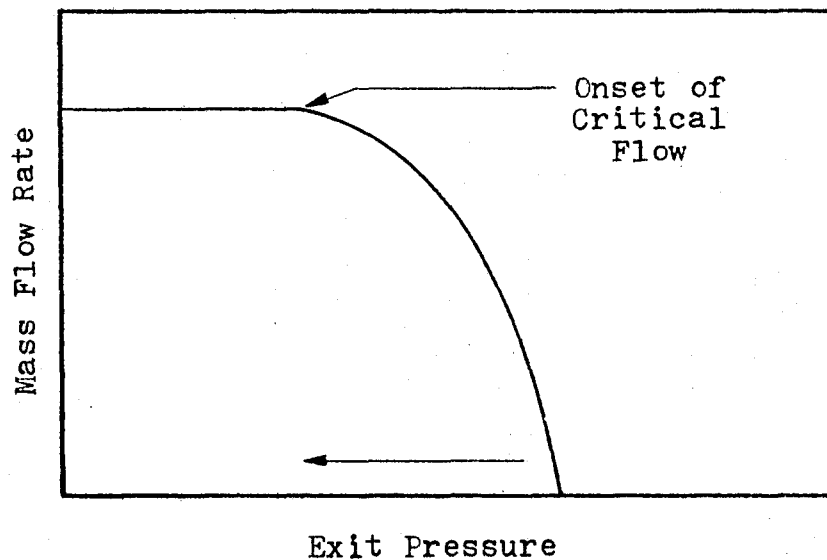
Exit Pressure

Fig. 2-2b.   Variation of mass flow rate with exit pressure,
showing onset of critical flow.

drop. Under this condition equation (2.3) becomes

$$- \partial P / \partial z = G_1 \, \partial u_1 / \partial z + G_g \, \partial u_g / \partial z \qquad (2.7)$$

The mass quality is defined as

$$x = G_g / (G_g + G_1) \qquad (2.8)$$

Combining equations (2.6), (2.7) and (2.8) gives

$$G_c = \left[- \frac{\partial}{\partial P} (x u_g + (1-x) u_1) \right]^{-1} \qquad (2.9)$$

Using the following relationships

$$(1-x) \, G = (1-\alpha) \, u_1 / v_1 \qquad (2.10)$$

$$x \, G = \alpha \, u_g / v_g \qquad (2.11)$$

$$u_g = S \, u_1 \qquad (2.12)$$

where S is the slip ratio, one derives

$$\alpha = x \, v_g / (S(1-x)v_1 + x \, v_g) \qquad (2.13)$$

By way of equations (2.10), (2.11) and (2.13), eliminating u_g and u_1 in equation (2.9) yields

$$G_c = \left[- \frac{\partial}{\partial P} \left(\frac{[S(1-x)v_1 + xv_g][xS + (1-x)]}{S} \right) \right]^{-\frac{1}{2}} \qquad (2.14)$$

where the expression is to be evaluated at the critical flow plane. This is a general expression for the two-phase critical mass flux. If the flow is adiabatic and two-component, the only effective interfacial process is interfacial momentum

transfer, that is the degree to which each phase is accelerated, represented by $\partial S / \partial P$.

In the homogeneous model for two-phase flow, the slip ratio is unity as both phases are considered to move at the same velocity. Under this condition equation (2.14) becomes

$$G_c = \left[- \frac{\partial}{\partial P} \left(v_1(1-x) + xv_g \right) \right]^{-\frac{1}{2}} \tag{2.15}$$

This model consistently underpredicts the critical flow rate (7).

Fauske (8) presented a separated flow model for critical flow with which he developed a relation for the slip ratio. The pressure gradient is assumed to have a maximum but finite value at the onset of critical flow. By way of this maximizing principle, he obtained for the slip ratio

$$S = \left(v_g / v_1 \right)^{\frac{1}{2}} \tag{2.16}$$

to give for equation (2.14)

$$G_c = \left[- \frac{\partial}{\partial P} \left(2x(1-x)(v_1 v_g)^{\frac{1}{2}} + v_1(1-x)^2 + v_g x^2 \right) \right]^{-\frac{1}{2}} \tag{2.17}$$

The conditions for this model are best satisfied by the annular flow regime. However it has been successfully applied to other regimes in steam-water flows over a wide range of qualities (5, p. 340). Fauske suggested that the apparent success of his model in non-annular regimes was due to high slip ratios compensating for non-equilibrium effects (9).

Fauske (9) considered that a better critical flow

model could be developed for non-annular regimes. He subsequently proposed a model based upon homogeneous flow with a local slip that was a function of the pressure. An empirical fit to air-water critical flow data in a straight tube gave the following relation for the slip ratio

$$S = 0.17 \, x^{0.18} \, (\, v_g / v_l \,)^{\frac{1}{2}} \qquad (2.18)$$

With this relation, equation (2.14) simplifies to

$$G_c = \left[-\frac{\partial}{\partial P} \, (\, x(1-x)(v_l v_g)^{\frac{1}{2}} \Theta + v_l(1-x)^2 + v_g x^2 \,) \right]^{-\frac{1}{2}} \qquad (2.19)$$

where

$$\Theta = 0.17 \, (\, x^{0.18} + x^{-0.18} \,)$$

This model has been successfully applied to low pressure steam-water data (10). Its success suggests that one-component two-phase flows behave in a two-component fashion at the critical flow plane, that is there is no flashing or mass transfer between the phases. Such behaviour has also been observed with separated flow models (6). Fauske's homogeneous model has found application in critical flow in an annular venturi, thus suggesting that the phenomenon is independent of the test section geometry (11).

If one assumes that the quality is constant, the liquid incompressible and the gas ideal, equations (2.15), (2.17) and (2.19) can be further simplified. Under these conditions the three models are given by equations (2.20), (2.21) and (2.22) as listed in Table 2-1. The models are

Table 2-1.   Models for the Prediction of Two-Phase Critical Flow Rates

Homogeneous Flow Model:

$$G_c = (v_g x/P)^{-\frac{1}{2}}$$

(2.20)

Fauske Separated Flow Model:

$$G_c = (\,(v_g/P)\,[x^2 + (1-x)(x)(v_1/v_g)^{\frac{1}{2}}]\,)^{-\frac{1}{2}}$$

(2.21)

Fauske Homogeneous Flow Model:

$$G_c = (\,(v_g/P)\,[x^2 + (1-x)(x)(v_1/v_g)^{\frac{1}{2}}(1+\ominus^2)/(2\ominus)]\,)^{-\frac{1}{2}}$$

(2.22)

where $\ominus = 0.17\,(x)^{0.18}$

All properties to be evaluated at the critical flow plane.

plotted for comparison in Figure 2-3. Fauske's separated flow model and the homogeneous flow model are seen to represent the upper and lower limits, respectively, of the critical flow rate.

These three models, the homogeneous model, Fauske's separated flow model and Fauske's homogeneous flow model, are representative of the numerous models available for critical flow prediction. In summary, they neglect frictional and gravitational pressure drops and assume thermal equilibrium and equal phase pressures. They are most appropriate for two-component flows. These models are not recommended for use in metastable systems such as short tubes and orifices where non-equilibrium effects are important.

2.3 Wall Shear Stress Measurements

The wall shear stress is obtained with the electro-chemical method. This method directly measures the rate of mass transfer to an electrode mounted flush with the test section wall. An analytical expression is required to link the mass transfer coefficient with the wall shear stress. A detailed study of the method and its application in the measurement of wall shear stress in two-phase flow, as well as the details of the ferricyanide electrolyte system, is given in an additional report by the author (12). The use of the iodine electrolyte system is discussed by McConagy (13). A comprehensive review of the electrochemical method is given by Mizushina (14). The discussion presented here will briefly present the defining equations of the method and the expression
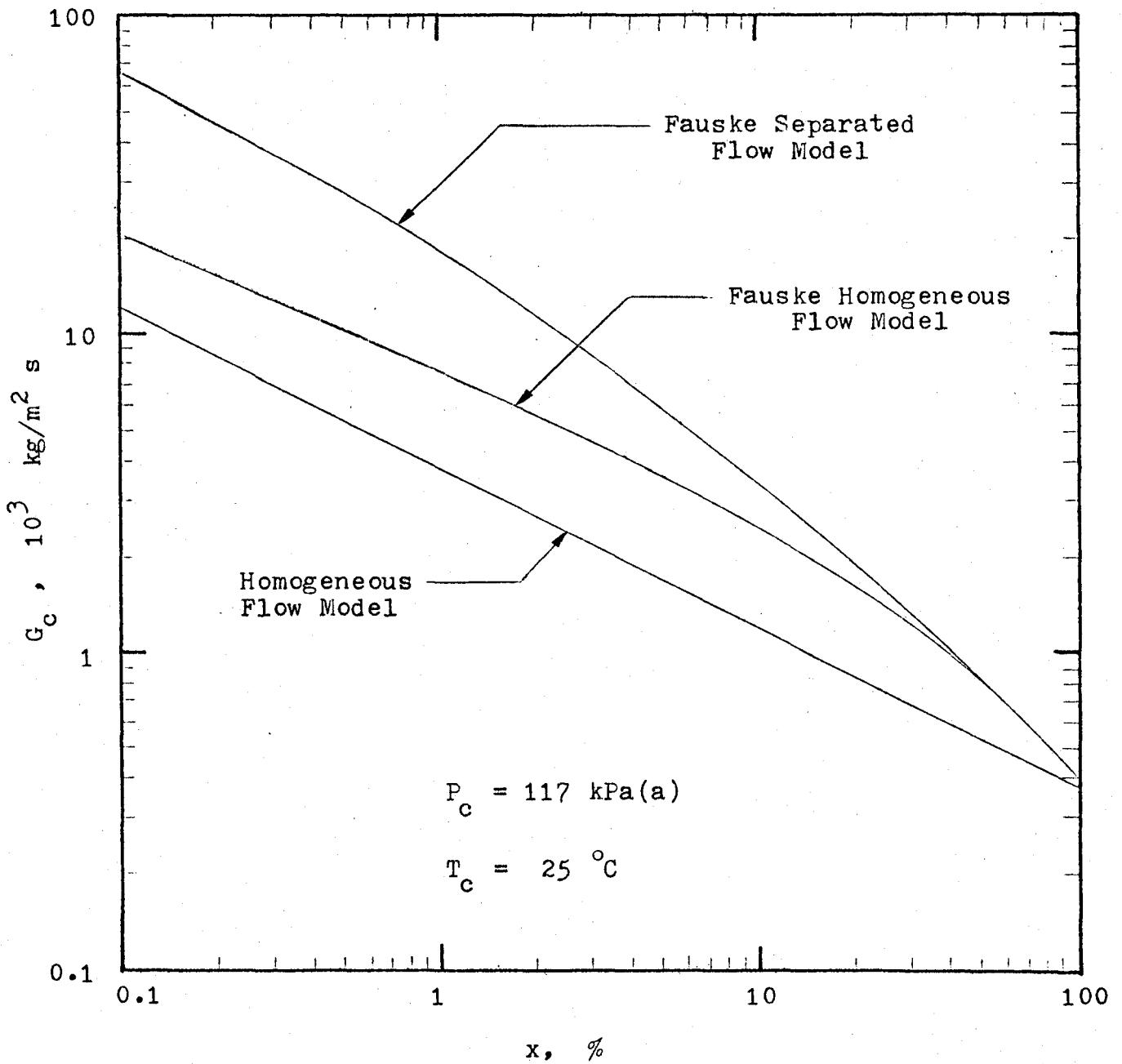
Fig. 2-3.   Calculated critical mass flux of an air-water flow.

used to calculate the wall shear stress. Refer to Figure 2-4 for illustration.

2.3.1 Electrochemical Method

The electrochemical method involves mounting electrodes at the wall to make up an electrochemical cell and circulating an electrolyte through the test section. As will be explained the cell current is a direct measure of the mass transfer coefficient.

The rate of mass transfer from the bulk of a solution to the surface of an electrode is governed by three mechanisms:

1. Transport by convection
2. Transport by diffusion due to the concentration gradient.
3. Transport by migration due to the potential field.

Two electrochemical systems are considered in this investigation. The first is iodine in excess potassium iodide. The chemical reactions are

At the cathode: $I_3^- + 2e^- \rightarrow 3I^-$

At the anode: $3I^- \rightarrow I_3^- + 2e^-$
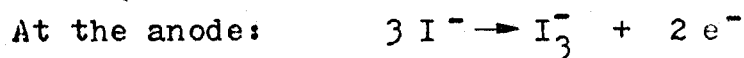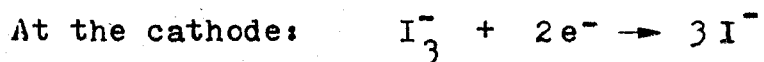
This system is illustrated in Figure 2-4. The second system is potassium ferri- and ferrocyanide in excess sodium hydroxide. The chemical reactions are:
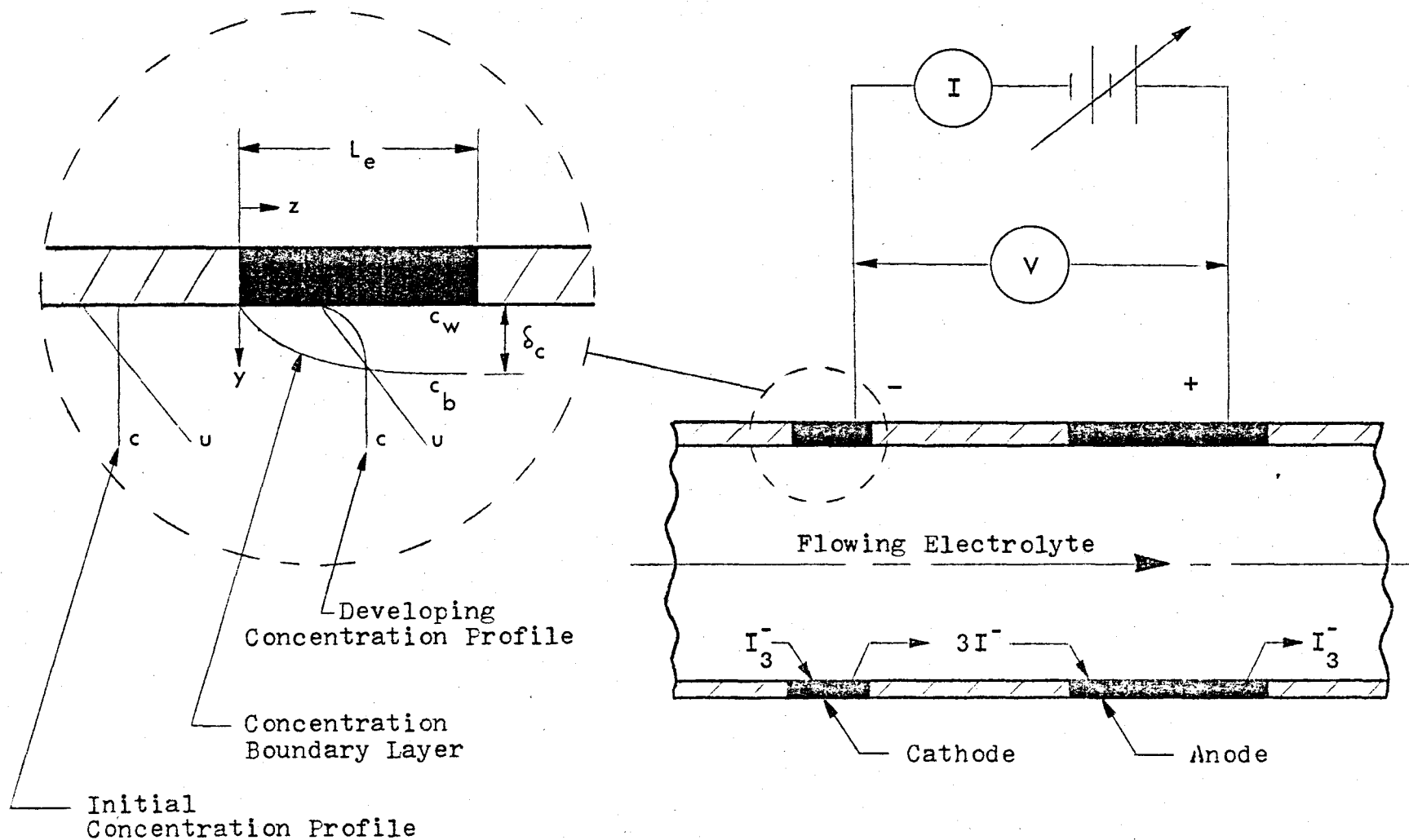
Fig. 2-4.   Basic electrochemical cell and development of the concentration boundary layer for the electrochemical method.

At the cathode: $Fe(CN)_6^{-3} + e^- \rightarrow Fe(CN)_6^{-4}$

At the anode: $Fe(CN)_6^{-4} \rightarrow e^- + Fe(CN)_6^{-3}$
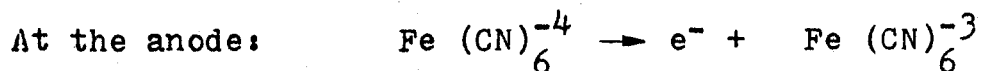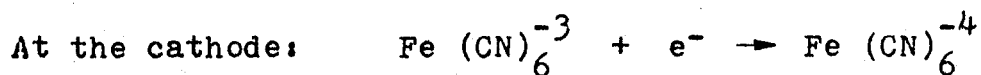
In both systems, complementary reactions occur at the anode and cathode. Thus the bulk concentration is constant, there is no actual deposition at the electrode and the net bulk flow to the electrodes is zero. As a result, transport by convection can be neglected. In addition, the presence of an excess indifferent electrolyte, such as the potassium iodide which is used in molar concentrations in contrast with the centimolar concentrations of iodine, reduces the potential gradient at the electrode surface to zero. Consequently transport by migration can be neglected. By making the surface of the anode much larger than that of the cathode, the limiting reaction takes place at the latter. Finally, by increasing the applied voltage in small steps and measuring the current, a polarization curve is obtained. Experimental polarization curves for different flow rates in single-phase flow are given in Figure 2-5 (12). The plateaus on the curves represent the limiting currents, the points at which the concentration at the surface of the electrode is zero.

Under all these conditions the electrochemical cell is polarized and diffusion-controlled. Faraday's law may then be combined with the definition of the mass transfer coefficient to give (12)

$$K = I_\ell / (n F a_e c_b) \qquad (2.23)$$
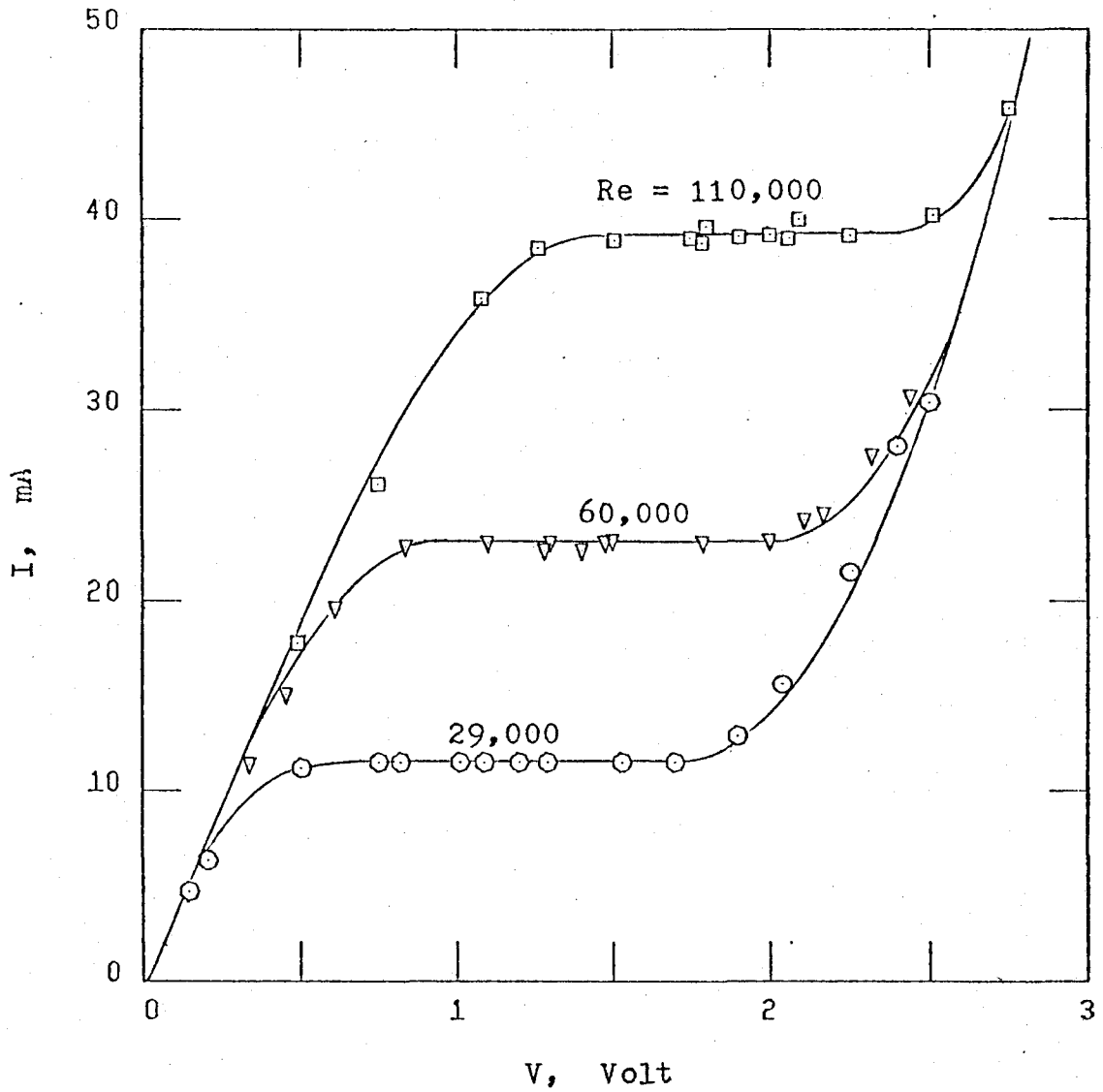
Fig. 2-5. Typical polarization curves obtained in single-phase flow.

where $n = 2$ for the iodine system, $n = 1$ for the ferricyanide system, a_e is the surface area of the cathode and c_b is the bulk concentration of the ferricyanide or iodine. Thus the mass transfer coefficient is given directly by the limiting current.

2.3.2 Shear Stress and Mass Transfer at the Wall

When the electrolyte reaches the electrode, a concentration profile begins to develop as shown in Figure 2-4. The initial uniform distribution changes to one exhibiting a steep gradient at the wall. The following assumptions are made to enable analysis of the mass transfer within the concentration boundary layer.

1. The electrolyte properties are constant.

2. The surface concentration is uniform with $c_w = 0$.

3. The bulk concentration is undisturbed.

4. Mass transfer is due to diffusion alone in the y direction.

5. Wall curvature is neglected.

6. The dominant velocity component is in the z direction and the velocity gradient is linear with $u = s\,y$.

The last two assumption rely upon the fact that the boundary layer is very thin for systems with high Schmidt numbers, typically $\delta_c^+ < 1$ for $Sc > 1,000$.

Under these assumptions a mass balance gives (12)

$$s \, y \; \partial c / \partial z \; = \; D \; \partial^2 c / \partial y^2 \qquad (2.24)$$

By setting

$$x \; = \; y \left[s / (9 \, z \, D) \right]^{1/3} \qquad (2.25)$$

equation (2.24) can be transformed to

$$d^2 c / dx^2 \; + \; 3 \, x^2 \, dc / dx \; = \; 0 \qquad (2.26)$$

The boundary conditions are

$$c \; = \; c_w \qquad \text{at} \qquad x \; = \; 0$$

$$c \; = \; c_b \qquad \text{at} \qquad x \rightarrow \infty$$

Leveque (15, pp. 363-367) first showed the solution to this problem to be

$$c \; = \; \left[(c_b - c_w) / 0.893 \right] \int_0^x \exp(-x^3) \, dx \; + \; c_w \qquad (2.27)$$

The mass transfer coefficient is defined by

$$k \; = \; \left[D / (c_b - c_w) \right] (\partial c / \partial y)_{y=0} \qquad (2.28)$$

The law of the wall, $T_w = s \mu$, together with equation (2.27) and (2.28) can be combined to give for the local mass transfer coefficient

$$k \; = \; (D / 0.893) \left[T_w / (9 \, D \mu_1 \, z) \right]^{1/3} \qquad (2.29)$$

This is referred to as the Leveque solution for developing

mass transfer. After integration over the length of the cathode, it can be rearranged to yield the wall shear stress in terms of the average mass transfer coefficient as

$$\tau_w = 1.898 \ (K)^3 \ L_e \ \rho_1 \ (Sc)^2 / \ \nu_1 \qquad (2.30)$$

If the electrode is a wire, the effective length is given by (14)

$$L_e = 0.8136 \ d_e \qquad (2.31)$$

The boundary layer becomes fully developed if the electrode is long enough. Numerous expressions have been derived for the fully developed mass transfer coefficient. Shaw and Hanratty's (16) relation is considered to be the most accurate for turbulent pipe flow. In terms of the wall shear stress, their expression is

$$\tau_w = 126.5 \ K_\infty^2 \ \rho_1 \ (Sc)^{1.408} \qquad (2.32)$$

The boundary layer is considered fully developed at $L^+ > 1,000$ for the local, and $L^+ > 10,000$ for the average mass transfer coefficient.

Thus the wall shear stress can be calculated from the measured mass transfer coefficient with equation (2.30) if $L^+ < 1,000$ and with equation (2.32) if the condition is fully developed. Though these expressions were originally derived for single-phase flows, they have been successfully applied to two-phase flows (12).

2.4   Void Fraction Measurements

A traversing gamma densitometer is used to measure the average cross-sectional void fractions. The technique is based upon the principle that a homogeneous medium will absorb or attenuate a monoenergetic collimated beam of constant intensity gamma radiation exponentially with increasing thickness of the absorption medium

$$\phi = \phi_o \exp (-\mu_a t) \qquad\qquad (2.33)$$

where ϕ_o is the unattenuated beam intensity. The linear absorption coefficient is a function of the medium material and gamma or photon energy. By passing a collimated beam of radiation from an external source through the test section and measuring the degree of attenuation of the emergent beam, the relative density and thus the void fraction of the mixture within the test section can be determined.

The apparatus for a densitometer operating in the counting mode is illustrated in Figure 2-6a. The intensity of the radiation is detected with a scintillation crystal and photomultiplier. The signal from the detector is amplified and a single channel analyzer serves to select the desired photon energy to be studied. The output signal can either be directly counted or converted to a voltage by a suitable ratemeter. The reading given by the densitometer is directly proportional to the intensity of the radiation reaching the detector, $N = C \phi$.
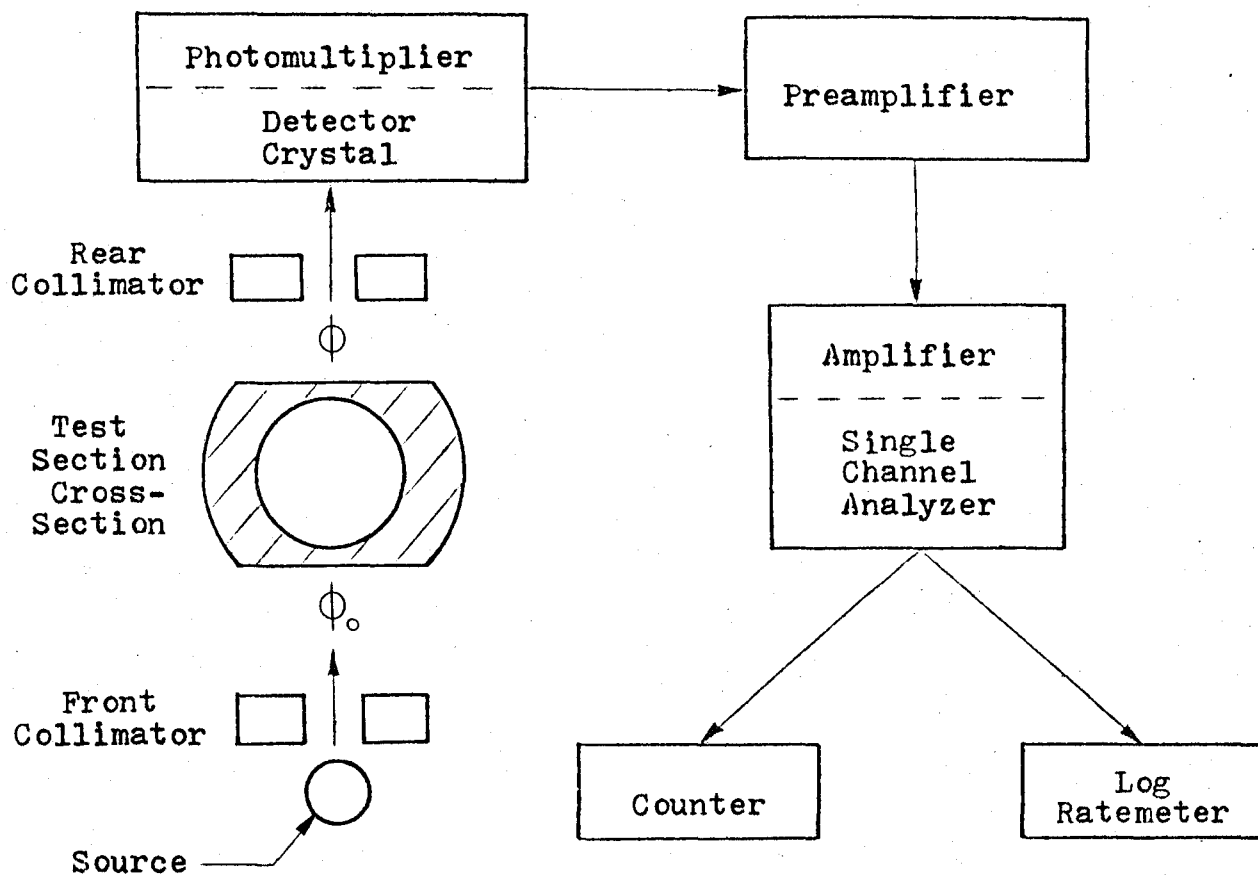
Fig. 2-6a.   Apparatus for the measurement of the void fractions
with a gamma densitometer.
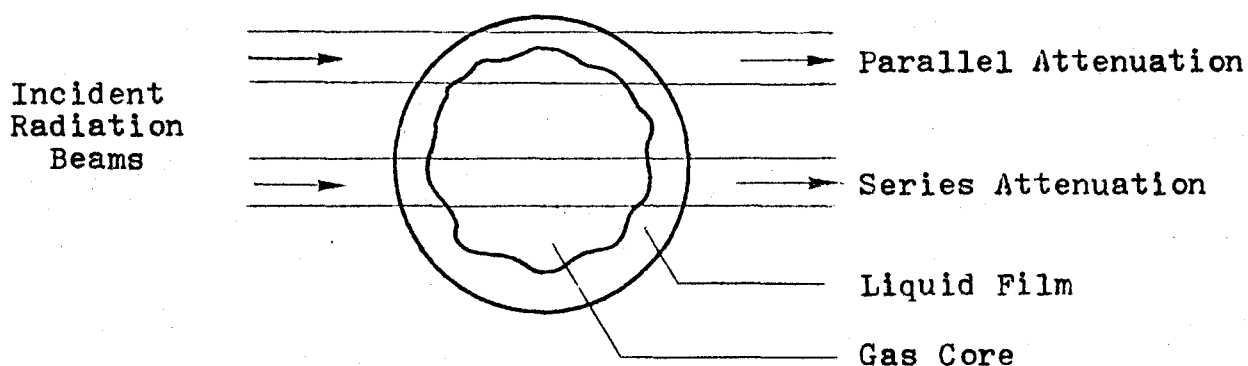
Fig. 2-6b.   Cross-section of an annular flow regime showing
the basic geometry of parallel and series attenuation.

The basic working equation is

$$\alpha = \left[\ln (\phi_{tp} / \phi_1) \right] / \left[\ln (\phi_g / \phi_1) \right] \quad (2.34)$$

where

ϕ_1 = beam intensity with liquid only in test section

ϕ_g = beam intensity with gas only in test section

ϕ_{tp} = beam intensity with two-phase mixture in test section

having assumed for equation (2.33)

$$\mu_a = \alpha \mu_a (gas) + (1 - \alpha) \mu_a (liquid) \quad (2.35)$$

Thus the void fraction is determined from individual measurements with the liquid phase, gas phase and two-phase mixture in the test section.

In its simplest form the technique uses a 'one-shot' method, in which a large diameter beam of radiation, that covers the entire cross-section of the test section, is used to determine the average cross-sectional void fraction. However the more accurate 'traversing' method is used in this study. This second method works with a much narrower beam in order to measure the average local void fractions and traverses both the detector and source across the test section to arrive at a transverse void fraction profile. The average cross-sectional void fraction is calculated by integrating across

the test section to give

$$\propto \; = \; 2/\Lambda \; \sum_{m=1}^{M} \; (\propto_y)_m \; [r^2 - y_m^2]^{\frac{1}{2}} \; (\triangle y_m) \qquad (2.36)$$

where

$(\propto_y)_m$ = average local void fraction at y_m

y_m = position from the centreline of test section

$\triangle y_m$ = distance between y_m and y_{m+1}, $\triangle y_m = 2r/M$

A number of points must be considered if this technique is to be used correctly. Equation (2.35) is based upon the assumption that the beam goes through the liquid and gas phases one after the other, that is by series attenuation, in which the phases can be represented as laminae perpendicular to the radiation beam. If in fact the phases are better represented as laminae arranged parallel to the beam, parallel attenuation, equation (2.34) would be incorrect. The working equation for parallel attenuation is

$$\propto \; = \; [(\phi_{tp}/\phi_1) - 1]/[(\phi_g/\phi_1) - 1] \qquad (2.37)$$

The two geometries are illustrated in Figure 2-6b with regard to an annular flow regime. These geometric factors require careful analysis of experimental results. The traversing technique, with its small beam, is least sensitive to phase geometry (17).

Another problem is that as the attenuated intensity varies nonlinearly with the void fraction, the fluctuations

in the output signal will also vary nonlinearly. If the signal is averaged, either by a counter or an averaging ratemeter, significant errors can arise when converting the averaged signal to the desired void fraction. This effect requires linearization prior to averaging or adopting the method of short time sampling, linearizing and final averaging of discrete samples of the signal. The former method is illustrated in Figure 2-6a, with a log ratemeter being used to linearize the signal.

For a more detailed review of the subject one should refer to Schrock (17). The report by Vogrin (18) gives the derivations of the equations presented in this section, as well as evidence of the higher accuracy of the traversing relative to the one-shot method.

CHAPTER 3

EXPERIMENTAL APPARATUS AND PROCEDURES

3.1   Loop

A test facility, designated the RD-13 freon-water loop, was modified for use in this study. The loop was originally designed for the development of two-phase flow instrumentation and was intended to use superheated freon and water to simulate steam-water flows. The simulation of the densities of steam-water mixtures is also intended to be a part of this investigation. Figure 3-1 illustrates that steam-water density ratios, for saturation pressures from 0.1 to 4 MPa(g), can be covered by air-water and Freon 12-water flows, for loop operating pressures from 10 to 500 kPa(g).

The basic RD-13 loop is illustrated in Figure 3-2. Both gas and liquid are circulated in closed loops. The liquid is circulated, by two centrifugal pumps operated in parallel, from the gas-liquid separation tank to the mixer, the test section, and then back to the separation tank. The gas is circulated, by a liquid ring compressor, from the separation tank to the storage tank, mixer, the test section and then back to the separation tank. The mixer is a pipe tee. Separate bypasses around the test section exist for the gas and liquid sides. Loop temperatures are controlled with water cooled heat exchangers on the liquid and gas delivery

30

P = operating pressure for air/water and

Freon 12/water mixtures,   kPa(g)

P = saturation pressure for steam/water

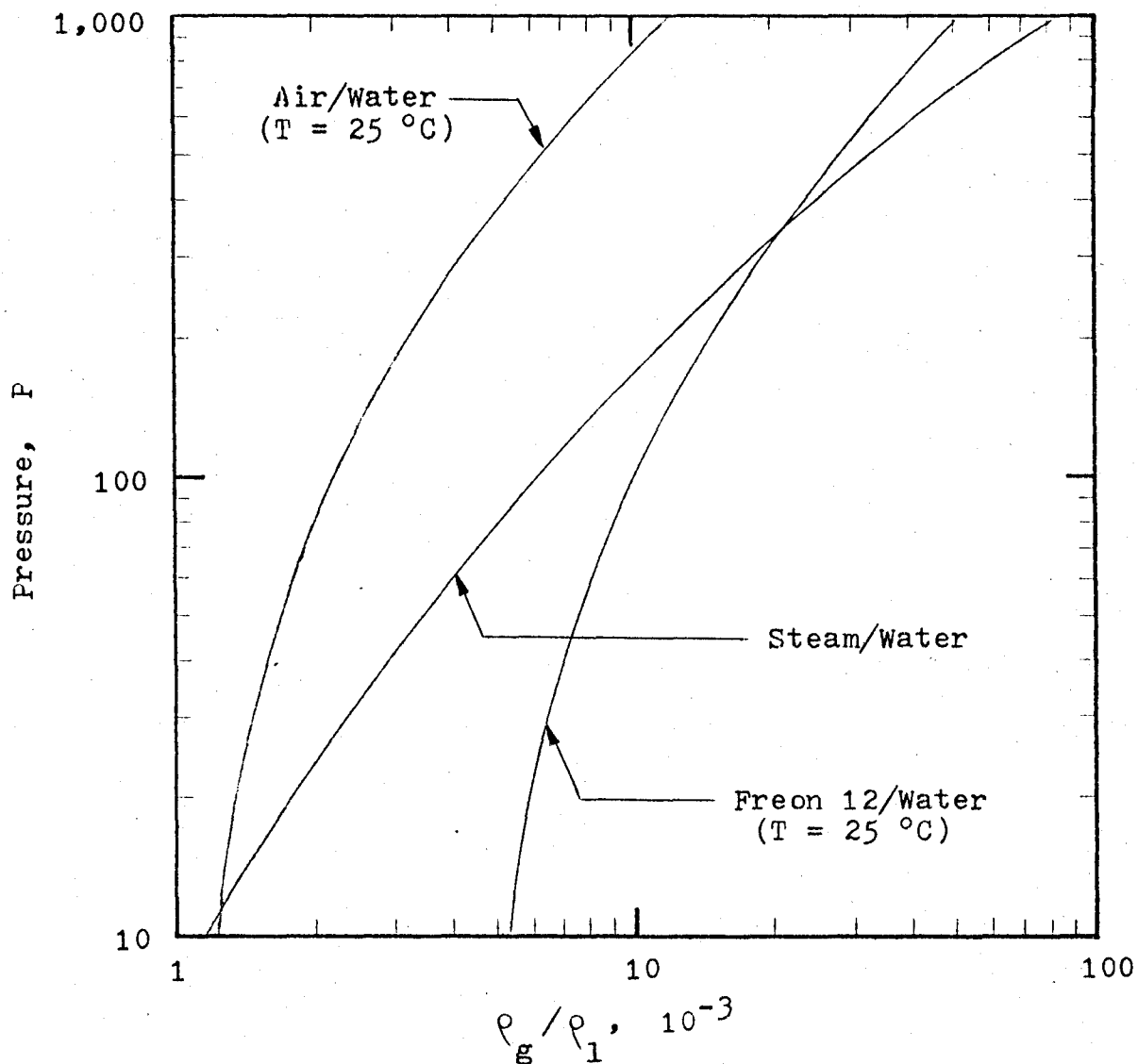mixtures,   kPa(g) x 10^{-1}

Fig. 3-1.   Comparison of the gas/liquid density ratios of
air/water, steam/water and Freon 12/water mixtures.
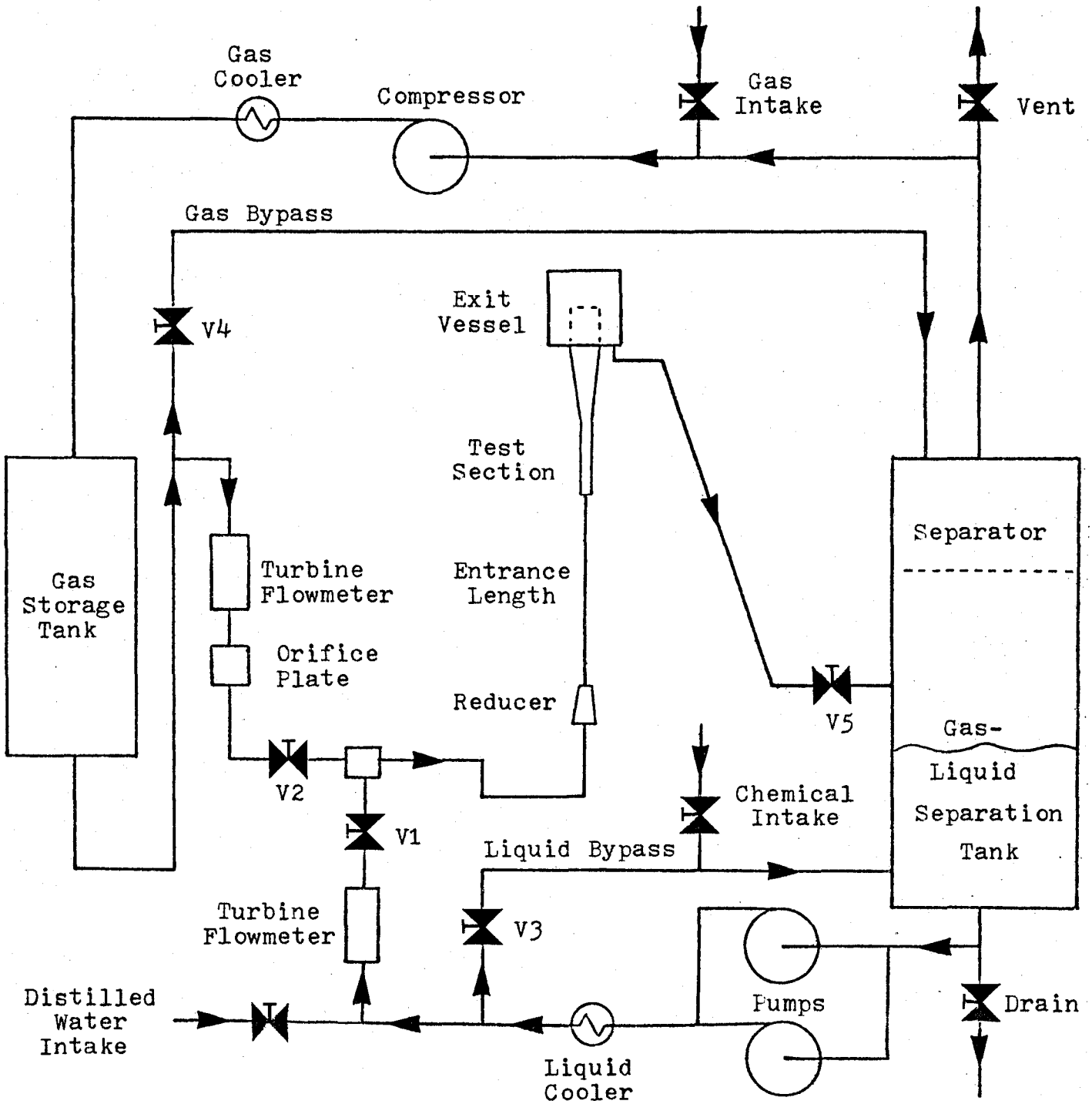
Fig. 3-2. RD-13 Loop in Vertical Test Mode.

lines.

All loop piping is 51 mm copper tube. The spool pieces, that is the piping for the flow rate instrumentation, liquid and gas coolers, are 51 mm stainless steel pipe. The separation of the liquid and gas is accomplished by gravity separation and a screen separator located at the top of the separation tank.

The test section is preceded by a 51 to 25 mm reducer, followed by a 3 m vertical run of 25 mm stainless steel pipe for full development of the flow. The test section exhausts to a 280 mm diameter stainless steel exit vessel which drains back to the separation tank.

Flow measurement is by turbine flowmeters and an additional orifice plate on the gas side. The desired flow rate is selected by setting the throttling valves V1 and V2, and adjusting the bypass flows with valves V3 and V4. To protect the operator from a possible rupture of the test section, the loop is controlled remotely and the test section observed through a plexiglass window.

Critical flow is attained by dropping the back pressure in the exit vessel with valve V5 until no change in the flow rate is detected. Figure 3-3 shows the range of critical flows available according to Fauske's homogeneous flow model, equation (2.21). The measured loop capacity is 6 l/s of liquid and 85 g/s of gas.

Provision is made for using air, nitrogen, Freon 12 or
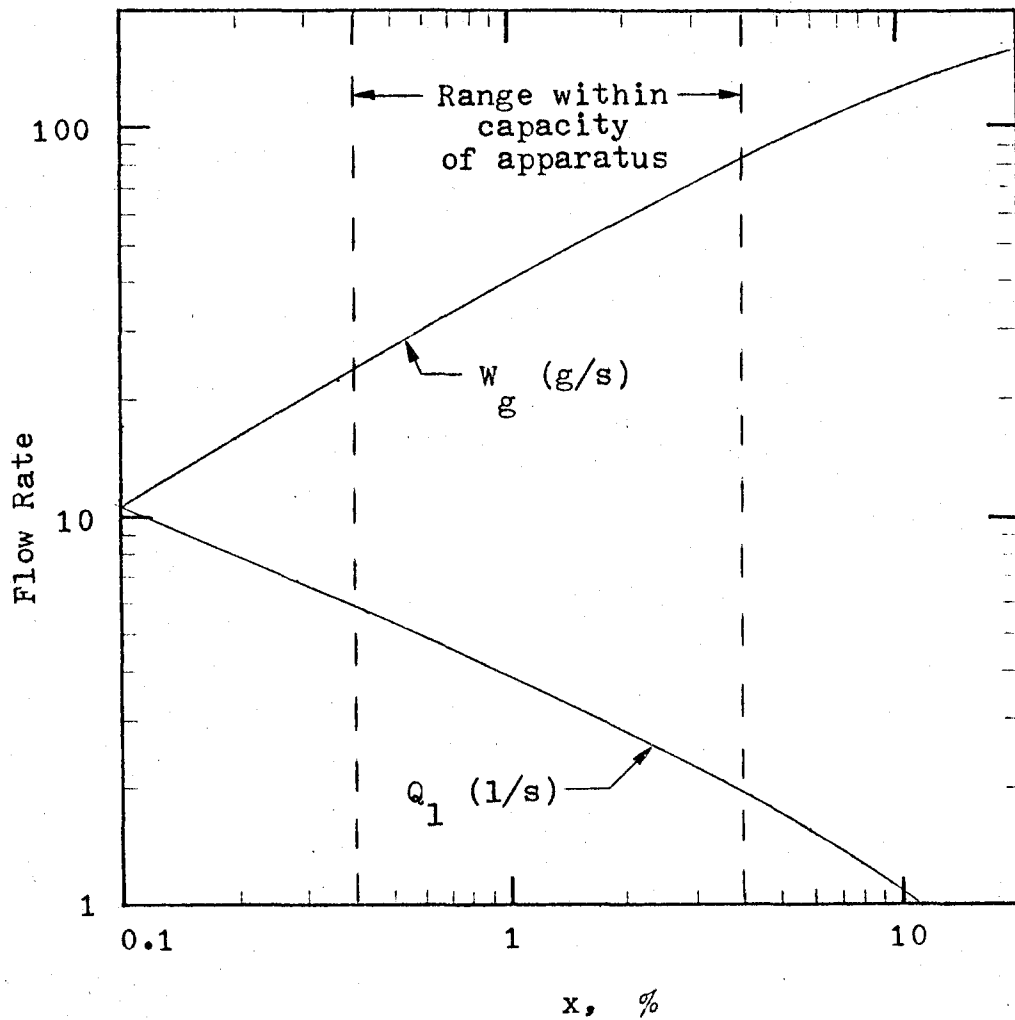
Fig. 3-3.   Gas and liquid flow rates required for the critical mass flux predicted by the Fauske homogeneous flow model, for an air-water flow in a 25 mm diameter tube.

Freon 22 as the gas phase. Distilled water is used for the liquid phase. An intake is provided for chemical addition to the water for operation wich an electrolyte. Originally potassium ferri- and ferrocyanide with sodium hydroxide was to be used as the electrolyte, due to its extensive use in the past and well established properties. However it was found that the hazardous nature of the sodium hydroxide, which is described in Appendix 2, would require further modifications to the loop and very restrictive operating and disposal procedures. On this basis it was decided to use iodine and potassium iodide as the electrolyte, there being no hazards associated with this system.

3.2   Test Section

The test section consists of a 25 mm constant diameter entrance section, 246 mm long, followed by a 7 degree straight diffuser, 363 mm long. The Lucite insulates the electrodes used for the wall shear stress measurements. In addition, its transparency enables visual study of the flow. Two opposing sides of the test section were machined to a minimum wall thickness of 6 mm to minimize parasitic attenuation of the gamma radiation beam of the densitometer.

As illustrated in Figure 3-4 the test section is instrumented with 20 pressure taps, 0.4 mm in diameter, and 19 platinum   wire cathodes, 0.5 mm in diameter. Thus individual measurements of the pressures and wall shear stresses can be made along the entire length of the test section in order
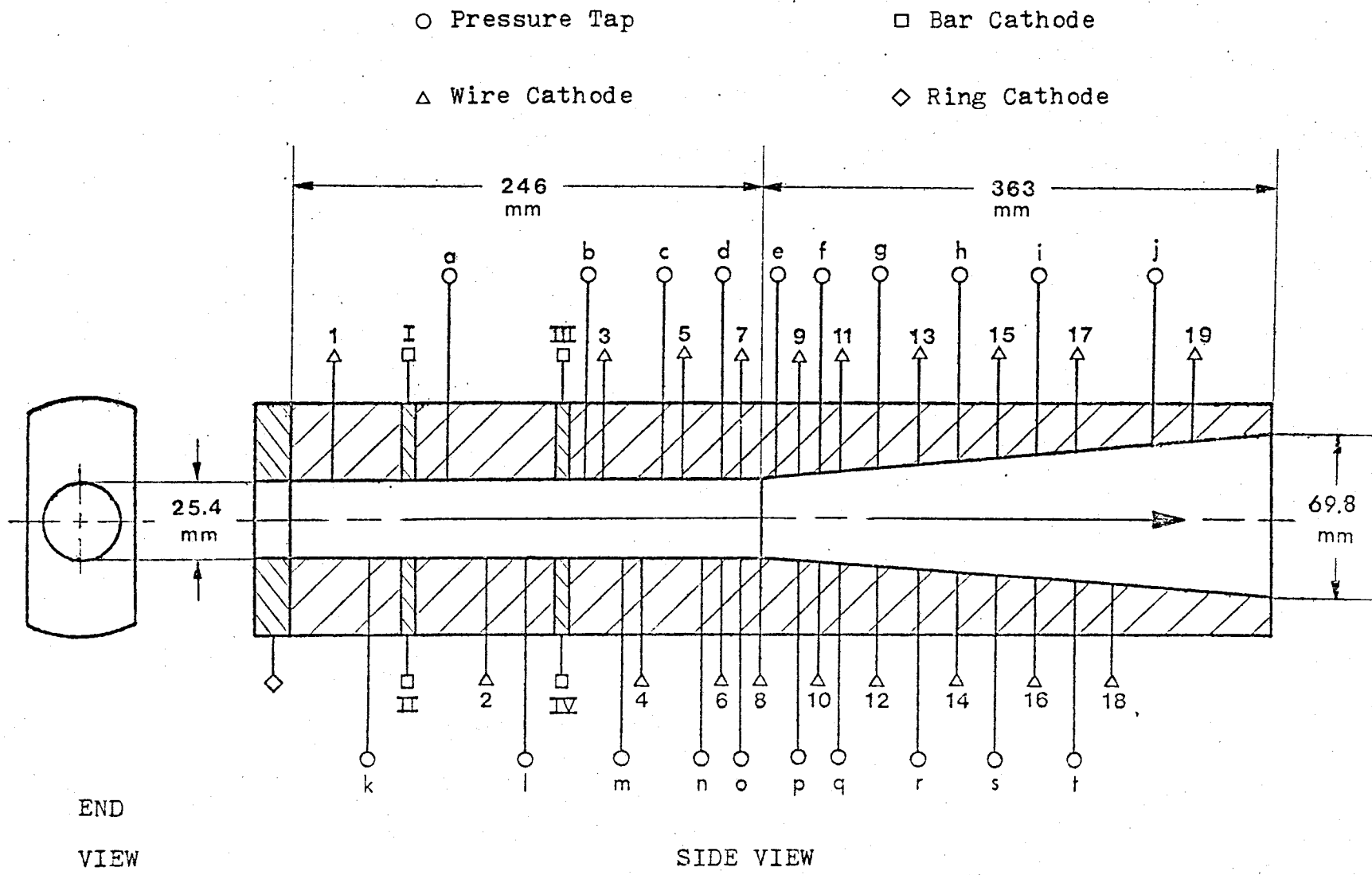
Fig. 3-4. Critical flow test section

to obtain the axial profiles. Four nickel bars and a nickel ring serve as reference cathodes for the wire cathodes. Downstream of the test section is a 76 mm stainless steel pipe, 152 mm long, which exhausts into the exit vessel. This exit pipe, together with the 25 mm pipe acting as a development length upstream of the test section, are used as anodes.

The choice of a diverging nozzle was made for the following reasons:

1. Instrumentation can be placed both upstream and downstream of the critical flow plane.

2. Flow separation from the wall and irreversible effects are minimized.

3. The pressure gradient is essentially one-dimensional. Thus the centreline pressure will not significantly differ from the pressure measured by the pressure taps.

4. It is more or less assured that the critical flow plane will be at the throat of the nozzle.

Two-dimensional flow and the exact location of the critical flow plane are problems encountered in straight tube studies. Their effects have led a number of investigators to mis-interpret their results (19). The presence of dissolved gases has also proved to be a complicating factor. But the low pressures and two-component nature of this investigation should negate this effect.

3.3   Wall Shear Stress Profile Measurements

The electrical hookup for the wall shear stress measurements is given in Figure 3-5a. The cathodes are operated on an individual basis, one wire and one ring or bar at a time. The currents are measured with sensing resistors. The voltages across these resistors are amplified and fed to a computer data acquisition system which serves to log the limiting currents, record the averages and ranges, and to calculate the mass transfer coefficients and wall shear stresses.

The procedure for determining the limiting currents of each cathode involves varying the voltage applied to the cell and noting the current. This serves to locate the position of the plateau on the polarization curve. The voltage is then centred on the plateau and the limiting current recorded after waiting for steady-state conditions to be achieved.

It is expected that the wire cathodes will be quite sensitive to edge effects, particularly failure of the electrodes from being perfectly flush with the test section wall. These effects will be corrected by using single-phase measurements of the bar and ring cathodes as reference values.

The electrochemical method is vulnerable to electrode contamination (12). Proper cleaning of the nickel electrodes and deaeration of the electrolyte is required for good accuracy. The gravity of these effects in this particular
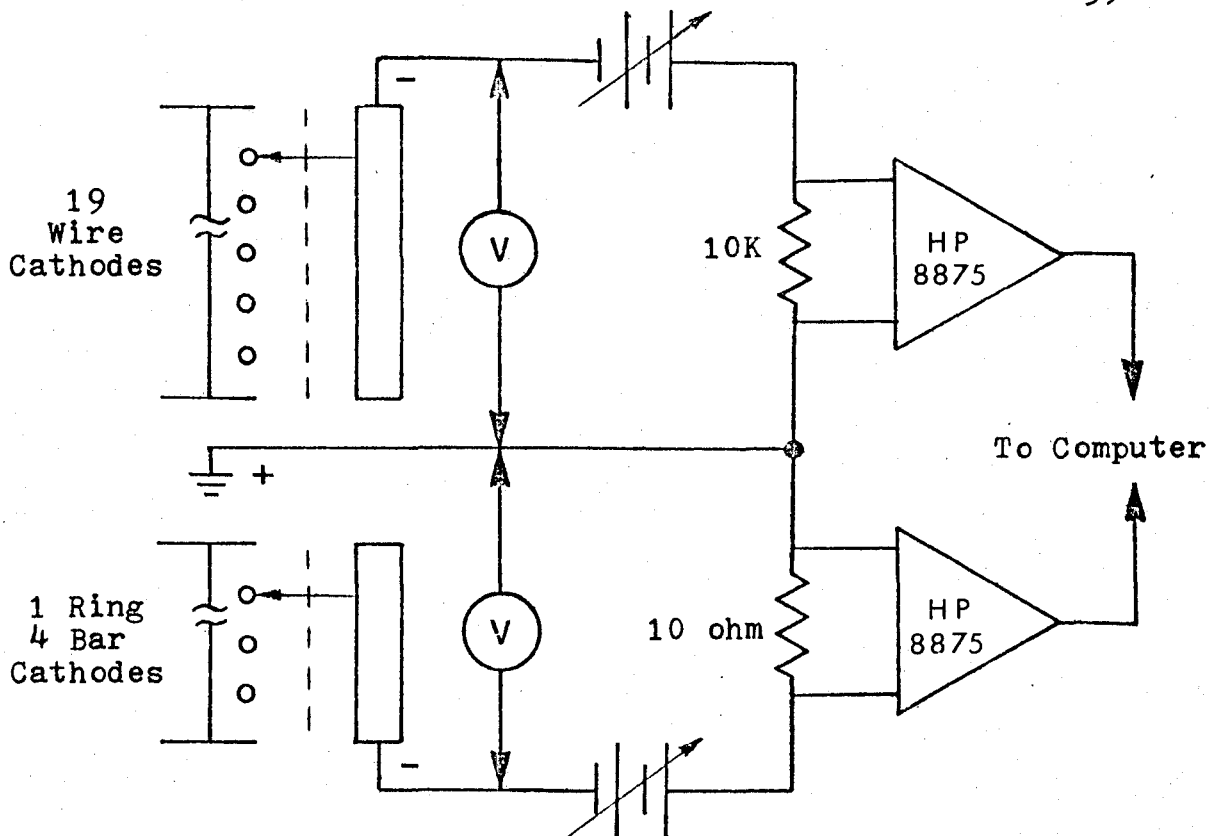
Fig 3-5a. Circuit for the measurement of the wall shear stresses.

SV = 8 Port Sampling Valve   PT = Pressure Transmitter
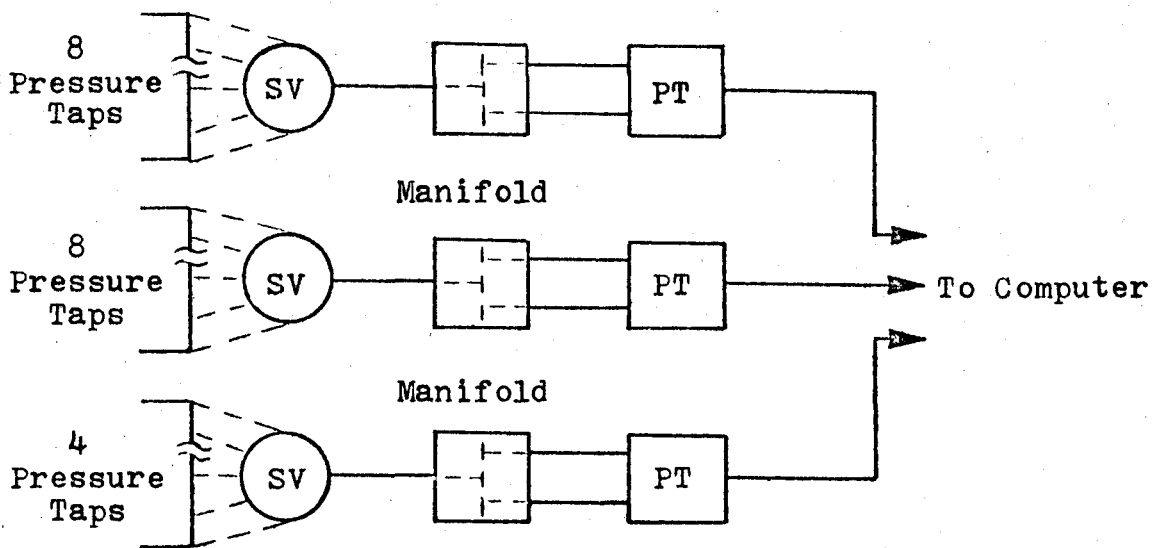
Fig 3-5b. Apparatus for the measurement of the pressure drops.

application of the method can only be determined after operating experience is gained with RD-13.

To determine the bulk concentration of the iodine, a sample is withdrawn from the loop. A standard titration with sodium thiosulphate and starch as the indicator is then performed.

3.4   Pressure Profile Measurements

The setup for the pressure measurements is given in Figure 3-5b. Nine port sampling valves are used in order that only 3 pressure transmitters be required to measure the pressure at the 20 pressure taps. The taps are connected to the valves with 1.6 mm stainless steel tubing. Rosemount pressure transmitters are used, and transducer drift is not expected to be a problem. The signals of the transmitters are fed to a computer acquisition system for logging and analysis. Manifolds are provided between the sampling valves and the transmitters for system flexibility. Is is intended to have the negative pressure ports of the transmitters open to atmosphere. Continuous line purging to ensure liquid filled lines will not be used. Instead occassion purging of the lines during the course of an experiment is to be adopted.

3.5   Void Fraction Profile Measurements

The apparatus for the measurement of the void fraction is given in Figure 2-6. The output of the ratemeter is fed to the computer data acquisition system for analysis.

The source is 20 mCi of Co^{57} with a peak photon energy of
122 keV. The properties of this source were judged to give
a suitable compromise between the high sensitivity of a low
energy source and the low parasitic absorption, in the test
section wall, of a high energy source. The detector is a
high efficiency sodium iodide crystal with integral photo-
multiplier.

A traversing mechanism enables the source and detector
to be positioned anywhere along the length of the test section
and centred at any cross-section. Thus both axial and trans-
verse profiles of the void fraction can be obtained. The
collimator is circular 4 mm in diameter. This can be
reduced in size, at the expense of the signal strength, to
achieve a more detailed transverse void fraction profile.

In accordance with equation (2.34), the 'empty' and
'full' channel void fractions will be recorded for each
measurement of the local void fraction. This will serve to
negate any drift in the densitometer or calibration problems.

Figure 3-6 shows the results of a simple experiment
which involved placing sheets of Lucite between the Co^{57}
source and the detector. The SCA was set to count photon
energies between about 110 and 150 keV. The validity of the
exponential attenuation relation, equation (2.33), is well
illustrated. This figure also shows the degree of centreline
attenuation that is experienced due to the test section wall
(13 mm of Lucite), with the 25.4 mm diameter portion full of
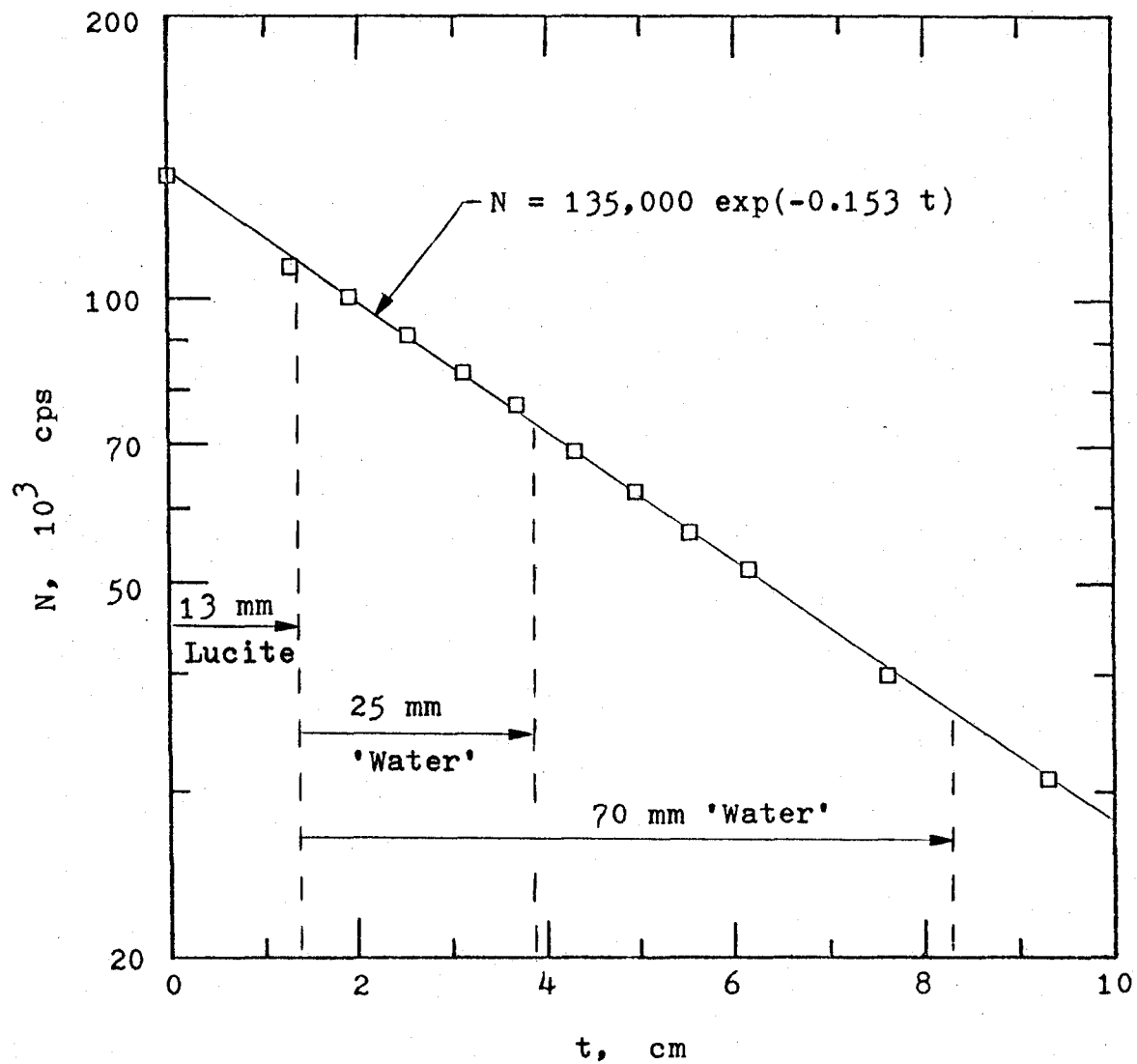
Fig. 3-6.   Gamma densitometer reading versus thickness of Lucite sheet placed between source and detector.

liquid (25 mm of 'water') and with the 69.8 mm diameter portion full of liquid (70 mm of 'water'). The linear absorption coefficient of Lucite is approximately the same as that for water. For 125 keV photons, $\mu_a = 0.160$ cm^{-1} in water.

CHAPTER 4

CONCLUSIONS

Preparations for an investigation of interfacial momentum transfer in two-phase two-component critical flows have been completed. A test facility has been constructed that will enable the measurement of flow rates, axial pressure profiles, axial and transverse void fraction profiles and axial wall shear stress profiles of critical gas-liquid flows in a vertical diverging nozzle under steady-state conditions. Experimental data gathered with this facility will be used to develop constitutive relations for interfacial momentum transfer.

This report has served to describe the required theory, apparatus, measuring techniques and procedures.

LIST OF REFERENCES

1. Collier, J.G., _Convective Boiling and Condensation_, McGraw-Hill (1972).

2. Banerjee, S., and Hancox, W.T., "Transient Thermo-hydraulics Analysis for Nuclear Reactors", 6th Int. Heat Transfer Conf., Toronto, Keynote Paper KS-23, 6, 311-337 (Aug. 1978).

3. Wallis, G.B., "Annular Two-Phase Flow. Part 1: A Simple Theory," _Trans. A.S.M.E., J. of Basic Eng._, 3, 59-72 (1970).

4. Boure, J.A., Fritte, A.A., Giot, M.M., and Reocreux, M.L., "Highlights of Two-Phase Critical Flow," _Int. J. Multiphase Flows_, 3, 1-22 (1976).

5. Hsu, Y.Y., and Graham, R.W., _Transport Processes in Boiling and Two-Phase Systems_, Hemisphere Pub. (1976).

6. Klingebiel, W.J., and Moulton, R.W., "Analysis of Flow Choking of Two-Phase, One-Component Mixtures," _AIChE J._, 17, 383-390 (1971).

7. Giot, M., and Fritte, A., "Two-Phase Two- and One-Component Critical Flows with the Variable Slip Model," _Progress in Heat and Mass Transfer_, 6, 651-670 (1972).

8. Fauske, H.K., "Contribution to the Theory of Two-Phase One-Component Critical Flow," _ANL-6633_ (Oct. 1962).

9. Fauske, H.K., "Two-Phase Two- and One-Component Critical Flow, _Proc. of Sym. on Two-Phase Flow_, Univ. of Exeter, Devon, 3, SG101 (1965).

10. Fauske, H.K., "Critical Two-Phase Flow," _Advanced Heat Transfer_, B.T. Chao Ed., Univ. of Illinois Press (1969).

11. Smith, R.V., Cousins, L.B., and Hewitt, G.F., "Two-Phase Two-Component Critical Flow in a Venturi," _AERE - R 5736_ (Dec. 1968).

12. Surgenor, B.W., "Mass Transfer and Shear Stress at the Wall for Cocurrent Gas-Liquid Flows in a Vertical Tube," M.Eng. Report, McMaster Univ., Hamilton (1978).

13. McConagy, G.A., "The Effect of Drag Reducing Polymers on Turbulent Mass Transfer, Ph.D. Thesis, University of Illinois, Urabana, Illinois (1974).

14. Mizushina, T., "The Electrochemical Method in Transport Phenomena," Advances in Heat Transfer, 7, 87-161 (1971).

15. Knudsen, J.G., and Katz, D.L., Fluid Dynamics and Heat Transfer, McGraw-Hill (1958).

16. Shaw, D.A., and Hanratty, T.J., "Turbulent Mass Transfer Rates to a Wall for Large Schmidt Numbers," AIChE J., 13, 689-696 (1977).

17. Schrock, V.E., "Radiation Attenuation Techniques in Two-Phase Flow Measurements," Two-Phase Flow Instrumentation, 11th Nat. ASME/AIChE Heat Transfer Conf., 24-35 (Aug. 1969).

18. Vogrin, J.A. Jr., "An Experimental Investigation of Two-Phase, Two-Component Flow in a Horizontal Converging-Diverging Nozzle," ANL-6754 (July 1963).

19. Henry, R.E.,"A Study of One- and Two Component Two-Phase Critical Flows at Low Qualities," ANL-7430 (Mar. 1968).

NOMENCLATURE

a	Surface area	m^2
A	Cross-sectional area	m^2
c	Chemical concentration	molar
C	Proportionality constant for densitometer	cm^2/photon
d	Diameter	m
D	Molecular diffusivity	m^2/s
F	Faraday's constant	A s
g	Acceleration due to gravity	m/s^2
G	Mass flux $= W/A$	kg/m s
I	Electrochemical cell current	mA
k	Local mass transfer coefficient	m/s
K	Space-averaged mass transfer coefficient	m/s
L	Length	m
n	Number of electrons transferred	
N	Gamma densitometer reading	cps
P	Pressure	kPa
Q	Volume flow rate	ml/s
r	Radius	m
s	Velocity gradient	1/s
S	Slip ratio	
t	Thickness of absorption medium	cm
T	Temperature	^{o}C
u	Flow velocity in z direction	m/s

u^*	Friction velocity	$= (\tau_w / \rho_1)^{\frac{1}{2}}$	m/s
v	Specific volume		m^3/kg
V	Electrochemical cell voltage		volt
W	Mass flow rate		g/s
x	Mass quality		%
y	Distance from wall, normal to the flow		m
z	Distance downstream, parallel to the flow		m

Greek Symbols

α	Void fraction	%
δ_c	Concentration boundary layer thickness	mm
μ	Absolute viscosity	kg/m s
μ_a	Linear Absorption coefficient	1/cm
ν	Kinematic viscosity	m^2/s
ρ	Density	kg/m^3
τ	Shear stress	N/m^2
ϕ	Intensity of radiation	photons/cm^2 s

Subscripts

b	Bulk
c	Critical
e	Electrode
g	Gas
i	Gas-liquid interface
ℓ	Limiting
l	Liquid

tp   Two-phase

w   Wall

∞ Fully developed

Dimensionless Numbers

f   Friction factor $= 2\,\tau_w / \rho\, u_b^2$

K^+ Mass transfer coefficient $= K/u^*$

L^+ Electrode length $= L_e\, u^* / \nu_1$

Sc   Schmidt number $= \nu_1 / D$

δ_c^+ Boundary layer thickness $= \delta_c\, u^* / \nu_1$

Re   Reynolds number $= u\, d / \nu$

APPENDIX 1

EQUIPMENT SPECIFICATIONS

A.1.1 Test Section

Main Body: material - Lucite

total length - 609 mm

diffuser angle - 7 degrees

diffuser length - 363 mm

entrance diameter - 25.4 mm

exit diameter - 69.8 mm

Ring Cathode: labelled - RC

material - Nickel 200

thickness - 12.70 mm

Bar Cathodes: labelled - I,II,III,IV

material - Nickel 200

thickness - 6.350 mm

width - I & II - 6.350 mm

III & IV - 12.70 mm

Wire Cathodes: labelled - 1 to 19

material - Platinum

diameter - 0.508 mm

Pressure Taps: labelled - a to t

diameter - 0.38 mm

The locations of the cathodes and pressure taps relative to the throat of the test section are given in Table A.1-1.

Table A.1-1. Location of Electrodes and Pressure Taps

Pressure Tap	Distance to Throat mm	Electrode	Distance to Throat mm
a	-120.65	1	-198.76
b	-44.45	2	-101.60
c	-19.05	3	-38.10
d	-6.35	4	-25.40
e	6.35	5	-15.88
f	19.05	6	-9.53
g	38.10	7	-3.18
h	66.23		
i	113.03	8	3.18
j	189.23	9	9.53
		10	15.88
k	-171.45	11	22.23
l	-82.55	12	31.75
m	-31.75	13	43.69
n	-12.70	14	55.88
		15	74.93
o	0.00	16	100.33
		17	125.73
p	12.70	18	163.83
q	25.40	19	214.63
r	49.53		
s	87.63	RC	-243.65
t	138.43		
		I	-145.42
		II	-145.42
		III	-63.50
		IV	-63.50

All distances are measured centreline to centreline.

Negative denotes distance upstream of the throat. Positive

denotes distance downstream of the throat.

A.1.2 <u>Loop</u>

Pumps: Two Bingham centrifugal pumps

1 x 1½ x 6¼ CAD

carbon steel construction

capacity - 7.5 1/s at 520 kPa(g)

5 HP , 3600 rpm electric drive

Compressor: Nash liquid ring compressor

Model 1253c, integral separator
and cooler

cast iron construction

capacity - 53 g/s at 690 kPa(g)

75 HP , 1800 electric drive

General: gas side volume - 1240 litres

liquid side volume - 410 litres

operating pressure - 600 kPa(g)

design pressure - 1,200 kPa(g)

operating temperature - 25 $^{\circ}$C

design temperature - 100 $^{\circ}$C

standard loop piping - 50.8 mm cooper

spool piece piping - 50.8 mm Sch 40 SS

valves and fittings - bronze

pressure relief valves - 860 kPa(g)

- 12.7 mm

Gas-Liquid Separation Tank: material - carbon steel

design pressure - 2,400 kPa(g)

design temperature - 427 $^{\circ}$C

capacity - 946 litres

operating liquid volume - 270 litres

Gas-Liquid Separator: type - circular screen separator

material - stainless steel

number of screens - 10

wire diameter - 1.5 mm

separation - 25 mm

pitch - 15 mm

Gas Storage Tank: material - carbon steel

design pressure - 4,100 kPa(g)

design temperature - 400 ^{o}C

capacity - 525 litres

Gas Cooler: type - single-pass shell and tube heat exchanger

material - stainless steel

total tube length - 16.25 m

tube outside diameter - 12.70 mm

cooling capacity - 4.5 kW

Liquid Cooler: type - single-pass shell and tube heat exchanger

material - stainless steel

total tube length - 11.2 m

tube outside diameter - 12.70 mm

cooling capacity - 7.5 kW

A.1.3 **Instrumentation**

Amplifiers: Hewlett Packard Model 8875A

Differential Amplifiers

Power Supplies: Sorenson QRB15-2 D.C. Variable

Power Supplies

Pressure transmitters: Rosemount Model 1151

                      Alphaline Pressure Transmitters

                      (differential capacitance)

Pressure Sampling Valves: Carle Gas Chromatogrphy

                      Model 2026, 8 position, 9 port

Turbine Flowmeters: Flow Technology

                      Models FT-321200-LB(s)

                      capacity - 15 l/s

Orifice Plates: type - flange, concentric,

                      thin plate, sharp edged

      labelled - OR1 to OR4

pipe inside diameter - 52.5 mm

bore diameter - OR1 - 15.00 mm

                OR2 - 21.00 mm

                OR3 - 25.00 mm

                OR4 - 28.50 mm

A.1.4   <u>Gamma Densitometer</u>

Source: 20 mCi Co^{57} (Amersham)

        active diameter - 4.2 mm

    collimator diameter - 5.0 mm

distance between source and detector - 145 mm

              window - 0.2 mm stainless steel

    principal energies - 122.1 keV (85 %)

              136.5 keV (11 %)

    half life - 270 days

Detector: Harshaw Sodium Iodide Scintillation Detector

Model 45HD1/2, Beryllium window

Crystal - 25 mm dia. by 6 mm thick

Preamplifier: Hewlett Packard Model 461A

Amplifier-Single Channel Analyzer: Conuclear Ltd C139

Ratemeter: Conuclear Ltd Model C138

Counter: Universal TSI Model 361

APPENDIX 2

CHEMICAL HAZARDS

The hazards associated with the operation of the electrochemical method using the potassium ferri- and ferrocyanide with sodium hydroxide electrolyte system are outlined below. There are no serious hazards associated with the iodine with potassium iodide electrolyte system. The level of precautions required to ensure safe operation of a loop utilizing this technique must be judged on the basis of the individual application.

The toxic nature of hydrogen cyanide is well known. As it is only a decomposition product associated with the potassium ferri- and ferrocyanide, it is unlikely that the threshold limit of 10 mg/m^3 for hydrogen cyanide vapour would be exceeded during normal operation. However if thought is given to neutralization of the electrolyte upon disposal, one must recognize that the hydrogen cyanide would no longer be in an alkaline solution and as a result, more significant quantities of HCN could be formed.

The sodium hydroxide presents a much greater hazard as it is extremely corrosive to human tissue, causing burns and deep ulceration. An unfortunate characteristic is that the chemical doesn't cause immediate pain when it comes in contact with the body, but it does start causing immediate

damage. Serious injury can result before one realizes that contact has been made. The greatest potential danger comes from a mist of sodium hydroxide. Such a mist could form in a two-phase system from a small leak in the piping with the pressurized gas phase acting as a propellant for the caustic solution. The effects of inhalation of such a mist can vary from mild irritation of the mucous membranes to severe pneumonitis. Particularly sensitive to damage are the delicate tissues of the eyes. The threshold limit for sodium hydroxide in air is 2 mg/m^3. Industrial practice is the requirement of respirators wherever mists _might_ be encountered. Figure A.2-1 illustrates the recommended protective clothing for the handling of sodium hydroxide, taken from the Caustic Soda Handbook as prepared by Dow Chemical of Canada.

In view of these hazards, the need for a fully enclosed loop with remote operation should be considered. Irregardless of the scale of the operation, an operator must ensure that he is wearing adequate protective clothing at all times.
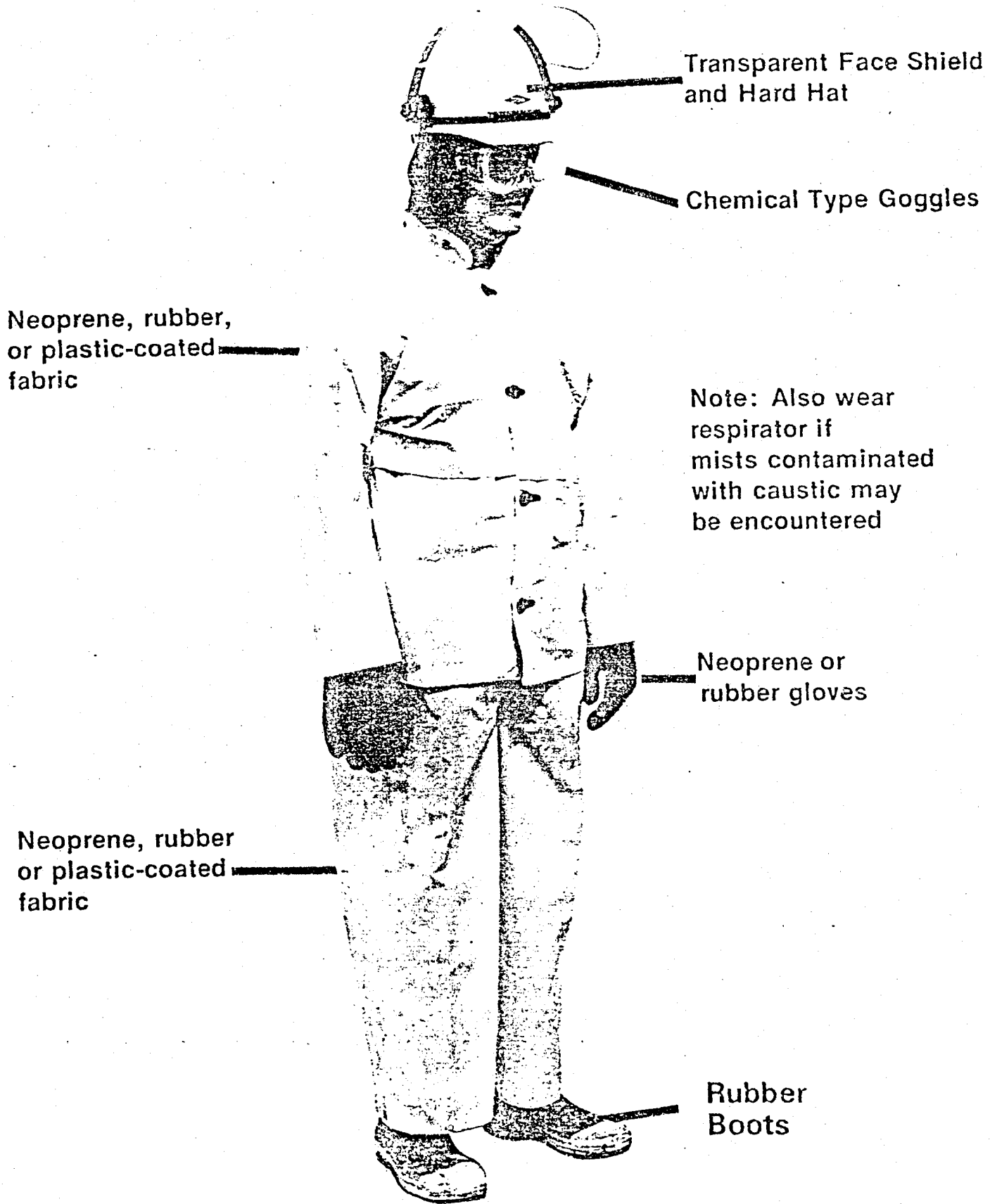
Fig. A.2-1. Protective clothing recommended for the handling of sodium hydroxide.